Nano Energy 75 (2020) 104879

Contents lists available at ScienceDirect

Nano Energy

journal homepage: http://www.elsevier.com/locate/nanoen

Tin disulfide piezoelectric nanogenerators for biomechanical energy harvesting and intelligent human-robot interface applications

Po-Kang Yang [a,e], Sui-An Chou [b,c], Ching-Hung Hsu [b,c], Roshan Jesus Mathew [b,c,f,g], Kuan-Hsuan Chiang [b,c], Jung-Yen Yang [d], Yit-Tsong Chen [b,c,*]

[a] Graduate Institute of Nanomedicine and Medical Engineering, College of Biomedical Engineering, Taipei Medical University, Taipei, 11031, Taiwan
[b] Department of Chemistry, National Taiwan University, No. 1, Sec. 4, Roosevelt Road, Taipei, 106, Taiwan
[c] Institute of Atomic and Molecular Sciences, Academia Sinica, P.O. Box 23-166, Taipei, 106, Taiwan
[d] National Applied Research Laboratories, Taiwan Semiconductor Research Institute, No. 26, Prosperity Road I, Hsinchu, 30078, Taiwan
[e] International Ph.D. Program in Biomedical Engineering, College of Biomedical Engineering, Taipei Medical University, Taipei, 11031, Taiwan
[f] Department of Engineering and System Science, National Tsing Hua University, Taiwan
[g] Nano-Science and Technology Program, Taiwan International Graduate Program, Academia Sinica, Taiwan

ARTICLE INFO

Keywords:
Two-dimensional materials
Tin disulfide
Piezoelectricity
Energy harvesting
Human-machine interface
Enabling sensing technology

ABSTRACT

Tin disulfide nanosheets (SnS_2 NSs), belonging to a new family of layered metal dichalcogenides, have evoked considerable attention in multidisplinary scientific applications because of their high electron mobility, excellent chemical stability, and wide accessibility to optoelectronic devices. However, despite the prediction of SnS_2 to possess excellent piezoelectricity, only very few attempts have been made to investigate the electromechanical characterisitcs of SnS_2. Herein, we report the experimental investigation of the intrinsic piezoelectricity of SnS_2 NSs, which were synthesized with a facile chemical vapor deposition (CVD) method. The prominent inverse piezoelectricity of SnS_2 NSs was measured *via* piezoresponse force microscpoy (PFM). To further evaluate the piezoelectric performance, SnS_2 NSs were integrated into a piezoelectric nanogenerator (PENG) device to display the energy harvesting and active sensing capabilities. Most importantly, the SnS_2 PENG device was utilized to explore the synchronous human-robot control of a smart sign language system, which demonstrates great potential for the future applications in human-machine interface and enabling sensing technology.

1. Introduction

The successful preparation of monolayer graphene by mechanical exfoliation from graphite in 2004 has triggered a significant amount of research in two-dimensional (2D) materials [1,2]. 2D materials possess a wide range of unique electrical [3], optical [4], mechanical [5], and thermal properties [6], which do not exist in their bulk counterparts. These unique properties have enlightened the development in lightweight, flexible, and high-performance device applications [7]. Particularly, the 2D transition metal dichalcogenides (TMDCs) with non-centrosymmetric structures have attracted great attention for their utilizations in the future electromechanical systems and piezoelectric devices [8].

The piezoelectricity of TMDCs has been a growing interest in recent years [9,10]. Piezoelectricity is generally unexpected to appear in bulk TMDC crystals because of their centrosymmetric structures. However, the high intrinsic piezoelectricities of monolayered or few-layered TMDCs, without centrosymmetry due to the absence of an inversion center, could be achieved by scaling down the material thickness to the atomic scale [10]. Recently, Wu et al. successfully fabricated the piezoelectric devices of molybdenum disulfide (MoS_2) with an odd number of crystal layers for energy conversion and piezotronics [11]. Han et al. used sulfur vacancy passivated MoS_2 nanosheets to enhance the performance of a MoS_2-based piezoelectric device by reducing free charge carriers to efficiently prevent the screening effect [12]. Nevertheless, it is noteworthy that the key to achieving a high-performance piezoelectric device is to explore a specific piezoelectric material of high intrinsic piezoelectric constant, facile fabrication process, and optimal sensitivity to external mechanical stimuli. Notwithstanding the reported piezoelectric devices that were mostly fabricated by mechanically exfoliated TMDCs, their comparatively low intrinsic piezoelectric constants could hinder them from producing high-performance

* Corresponding author. Department of Chemistry, National Taiwan University, No. 1, Sec. 4, Roosevelt Road, Taipei, 106, Taiwan.
E-mail address: ytcchem@ntu.edu.tw (Y.-T. Chen).

https://doi.org/10.1016/j.nanoen.2020.104879
Received 15 February 2020; Received in revised form 21 April 2020; Accepted 21 April 2020
Available online 15 May 2020

piezoelectric devices [11–14].

Other layered metal dichalcogenides have also been anticipated to exhibit excellent piezoelectricity, including molybdenum diselenide ($MoSe_2$), molybdenum ditelluride ($MoTe_2$), tungsten diselenide (WSe_2), and tin disulfide (SnS_2) [15]. Among them, SnS_2, predicted theoretically to possess a relatively high piezoelectric constant [15], is a promising candidate for a variety of applications, including photodetector [16], magnetics [17], catalytic reaction [18], and thermoelectric [19]. To date, however, only very few studies of the piezoelectricity of SnS_2 have been reported [20].

Herein, we report, for the first time, an experimental investigation of the piezoelectricity of few-layered tin disulfide nanosheets (SnS_2 NSs) synthesized with a facile chemical vapor deposition (CVD) method. The intrinsic out-of-plane piezoelectricity and the piezoelectric constant of SnS_2 NSs were measured by piezoresponse force microscopy (PFM). The as-synthesized SnS_2 NSs were further integrated into a piezoelectric nanogenerator (PENG) device for biomechanical energy harvesting and strain sensing applications. More interestingly, the self-powered SnS_2 NSs-based PENG devices were employed as a drive unit for the synchronous human-robot control platform of a smart sign language system. Our successful demonstration of the atomically thin, highly flexible, and multi-functional SnS_2 PENG devices has opened up a new avenue for diverse research fields, particularly in biomechanical energy harvesting, human-machine interface control, and enabling sensing technology.

2. Experimental Section

2.1. Synthesis of SnS_2 NSs

Few-layered SnS_2 NSs were grown on a Si substrate with 300-nm-thick SiO_2 *via* CVD reaction (Fig. 1a). The growth substrate was cleaned by sonication in acetone for 10 min, isopropanol for 10 min, and deionized water for 10 min, followed by drying with N_2 gas and O_2 plasma for 5 min. The growth substrates were face-down and above a ceramic boat containing 100 mg of tin oxalate (SnC_2O_4) powder (99.98%, Sigma-Aldrich), both of which were then loaded into a 1-inch diameter quartz tube located in a furnace system. A ceramic boat with 1 g of sulfur powder (99.98%, Sigma-Aldrich) was put in the upstream region near the edge of the furnace. The sulfur powder was sublimated at 200 °C with a heating belt. The furnace was gradually heated from room temperature to 600 °C in 19 min (Fig. S1 of the Supporting Information). During the synthetic reaction, the CVD system was maintained at 100 torr with an Ar flow of 100 sccm. After 10 min reaction, the furnace was rapidly cooled down to room temperature.

2.2. Materials characterization

An optical microscope (Olympus BX51 M) equipped with a charge-coupled device (Leica DFC495) was used for optical imaging. The surface topograph, material morphology, and elemental analysis of samples were conducted by AFM (Bruker Dimension Icon), SEM (JEOL JSM-7800F), and EDS (Oxford systems), respectively. XPS spectra were measured with an ESCA spectrometer (Escalab 250, VG Scientific) coupled with a monochromatic X-ray source (1486.6 eV Al Kα) and processed using CASA XPS software (v.2.3.17, Casa Software Ltd). The XPS spectra were calibrated against the binding energy of the C 1s signal at 284.60 eV of the adventitious carbon prior to the spectral measurements, which was also used as the reference energy to correct the background charging effect. The spectral background subtraction was made using the Shirley-Sherwood method. The quantitative elemental compositions were calculated by integrating the highest peak intensity and considering the atomic sensitivity factor of each element. Raman imaging was performed in a micro-Raman spectrometer (LabRAM HR, Horiba) composed of an optical microscope (Olympus CX41), a detector (Jobin Won Horiba S Drive-500 Syncernity), and a 532 nm laser of ~1

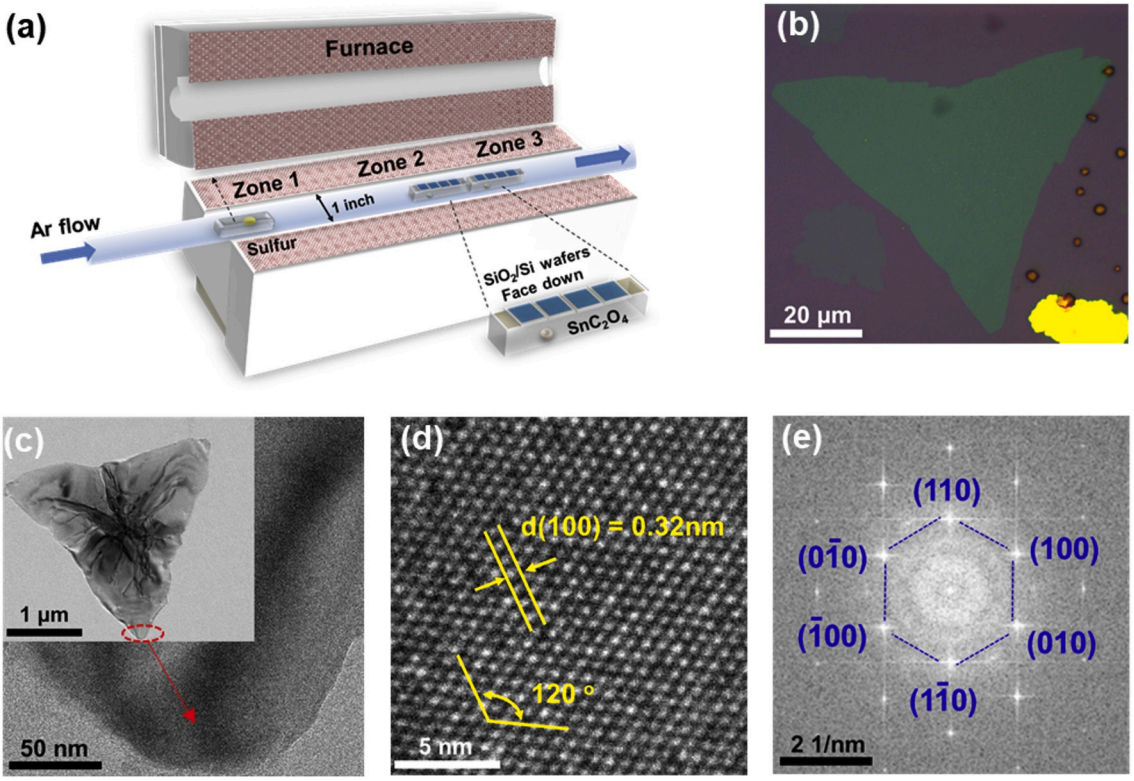

Fig. 1. (a) A schematic illustration represents the CVD system for the synthesis of few-layered SnS_2 NSs. The (b) optical image, (c) TEM image (with single few-layered SnS_2 NSs shown in the inset), (d) HR-TEM crystal structure, and (e) SAED pattern of the as-synthesized SnS_2 NSs were investigated for morphological and crystalline characterizations.

mW power guided through a 50X objective lens with the scattered light dispersed by a grating of 1800 g/mm. The data acquisition time for the Raman scan was 15 s and the first-order Raman scattering of Si at 520 cm^{-1} was used as a calibration reference. HR-TEM (Tecnai G2 F20 FEG-TEM) operating at 300 kV was used to examine crystal structures, of which the data were analyzed using Digital Micrograph software. PFM measurements were conducted by an AFM (Bruker Dimension Icon), in which the PFM images were obtained by contact mode with a tunable LS PR AC bias and the driving frequency at 15 kHz. The samples were tested near the resonant frequency of the vibrating cantilever, which exhibits the first Eigen mode in normal deflection at 287 kHz.

2.3. Piezoelectric coefficient of d_{33}

The measured PFM amplitude images of SnS_2 NSs were used to estimate the out-of-plane piezoelectric response qualitatively. To determine the d_{33} value of SnS_2 NSs, the vertical deflection of the used AFM cantilever is a key parameter to be obtained. We acquired the piezoelectric coefficient of d_{33} from the slope of applied AC voltage *vs.* amplitude plot *via* $d_{33} = (A_{LSPR} \cdot S_D)/(F_p \cdot V_{LSPR})$, where A_{LSPR} is the amplitude (mV), S_D is deflection sensitivity (nm/V), F_p is the facility parameter, and V_{LSPR} represents the external applied AC voltage (V).

2.4. Device fabrication

The CVD-grown SnS_2 NSs were transferred to a polyimide substrate with the assistance of polymethylmethacrylate (PMMA). The SnS_2 PENG devices were then fabricated with a standard photolithography process. A photomask of the electrode definition is shown in Fig. 3b, where the separation of electrodes in the narrowest claw region is 6 μm. The deposition of metal electrodes (30/70 nm-thick Cr/Au) was conducted in a thermal evaporator. Subsequently, the entire device was immersed into acetone for lift-off the residual photoresist. Finally, polydimethylsiloxane (PDMS) was served as an outer package material to cover the active region of the device and complete the fabrication of a SnS_2 PENG.

2.5. Output performance characterization

The piezoelectric outputs of SnS_2 PENGs were measured with a programmable electrometer (Keithley, Model 6514, 200 TΩ input impedance) and low-noise preamplifiers (Stanford Research System, Model SR570 and SR560). A commercial linear motor system was applied to provide the tunable external force and strain inputs.

2.6. 3D printed artificial robotic arms

A fully 3D printed robotic hand was produced by a commercial 3D printer machine from XYZ Printing Technology. The major printing material of polylactide (PLA) was processed at 208 °C with a well-known Fused Filament Fabrication (FFF) technique. The source of a printing model is from the Parloma project.

3. Results and discussion

The synthesis and characterization of few-layered SnS_2 NSs are shown in Fig. 1. The atomically thin SnS_2 NSs were synthesized on a SiO_2 (300 nm in thickness)/Si substrate *via* CVD reaction. Fig. 1a illustrates the experimental setup of the CVD system for high synthesis yields of SnS_2 NSs with the temporal reaction-temperature profiles during the CVD synthesis shown in Fig. S1. In the CVD reaction, tin oxalate (SnC_2O_4) and sulfur (S) powder were used as chemical precursors and argon (Ar) as carrier gas (with details described in Experimental Section). The furnace temperature was ramped up from room temperature to 600 °C in 20 min and maintained at 600 °C for 15 min during the SnS_2 crystal growth. The CVD reaction processes are summarized as follows.

$$SnC_2O_{4\ (s)} \rightarrow SnO_{\ (s)} + CO_{\ (g)} + CO_{2\ (g)} \quad (1)$$

$$2\ SnO_{\ (s)} + 5\ S_{\ (s)} \rightarrow 2\ SnS_{2\ (s)} + SO_{2\ (g)} \quad (2)$$

Fig. 1b shows a selected optical image of the as-synthesized few-layered SnS_2 NSs of a triangular shape with their sizes ranging from tens of micrometers to more than a hundred micrometers. To characterize the crystal structure of the few-layered SnS_2 NSs, low- and high-magnification transmission electron microscopy morphologies (TEM, Fig. 1c), high-resolution TEM image (HR-TEM, Fig. 1d), and selected-area electron diffraction pattern (SAED, Fig. 1e) were obtained to confirm the hexagonal crystal with the interplanar spacing of $d_{(100)} =$ 0.32 nm [21,22]. The homogeneous distribution of the chemical compositions of Sn and S in the as-synthesized SnS_2 crystal is demonstrated by EDX elemental mapping in Fig. S2a–b.

Atomic force microscopy (AFM), Raman spectroscopy, and X-ray photoelectron spectroscopy (XPS) were further applied to analyze the surface topograph, vibrational motions, and elemental compositions of the as-synthesized SnS_2 NSs. Shown in Fig. S3 are two selected SnS_2 NSs (optical images denoted by thin and thick, respectively, in the right inset of Fig. S3c) of ~4 nm (ca. 6 layers, AFM topograph in Fig. S3a) and ~40 nm (ca. 60 layers, Fig. S3b) in thickness, with a monolayer SnS_2 NS determined to be 0.6 nm thick previously [23]. In Fig. S3c, the Raman observation of a strong A_{1g} band at 315 cm^{-1} and a weak E_g signal at 205 cm^{-1} indicates the high-quality 2H–SnS_2 crystal, where the absence of E_g signal in the thin SnS_2 NSs could be due to the reduction of the in-plane scattering center [24,25]. In Fig. S4, XPS was employed to determine the elemental compositions and oxidation states of the constituent atoms in the as-synthesized SnS_2 NSs. While the observed signals of Sn $3d_{5/2}$ at 486.5 eV and Sn $3d_{3/2}$ at 494.9 eV are associated with the Sn^{4+} state, the peaks of S $2p_{3/2}$ at 161.5 eV and S $2p_{1/2}$ at 162.5 eV are related to the S^{2-} state [26–28].

Piezoelectricity, one of the fundamental properties of piezoelectric materials, is to develop electric charges on material surfaces under an external mechanical stress. We investigated the intrinsic piezoelectric property of SnS_2 NSs by piezoresponse force microscopy (PFM, illustrated in Fig. 2a), where the mechanical response of a tested sample is measured upon the vertical electric field applied through the PFM tip [29–32]. Fig. 2b displays the local AFM topograph of a tested SnS_2 crystal of ~2.5 nm in thickness, corresponding to four-layered SnS_2 NSs. Shown in Fig. 2c–e are the images of surface topograph, output amplitude, and output phase measured for the entire area of the four-layered SnS_2 NSs. The amplitude image of Fig. 2d displays an obvious piezoelectric response, reflecting the inherent out-of-plane piezoelectricity of the SnS_2 NSs. Interestingly, the gradient of amplitude images (i.e., the color change in Fig. 2f) is in nearly linear proportion to the applied tip voltages at 1–9 V, indicating the strong inverse piezoelectricity of SnS_2 NSs [30]. From the measured PFM data, the vertical (out-of-plane) piezoelectric coefficient (d_{33}) of SnS_2 NSs was determined to be ~5 pm/V (as shown in Fig. S5 with the calculations presented in Experimental Section). The reports for the space group of the SnS_2 crystal have been somewhat diverse. If according to a number of previous studies, [24,33–35], the 2H–SnS_2 crystal of a hexagonal structure possesses the space group of P-3m1. This observed vertical piezoelectric response in SnS_2 NSs originates from the strain gradient-induced flexoelectricity, because the out-of-plane piezoelectricity is not expected to be induced in the P-3m1 crystal by uniform strain [32,36,37]. Therefore, the out-of-plane piezoelectric coefficient measured in SnS_2 NSs should be called an effective d_{33}. It is also noted that apart from the intrinsic flexoresponse of a crystal itself, the out-of-plane piezoelectricity of a 2D crystal could be created by distorted crystal, structural defect, or substrate roughness, where the lattice distortion [38,39], atomic vacancy [40], or surface corrugation [40] in 2D structures was reported to yield a net dipole along the direction perpendicular to the lattice plane (i.e., out-of-plane polarization), consequently producing an out-of-plane piezoresponse. As compared in

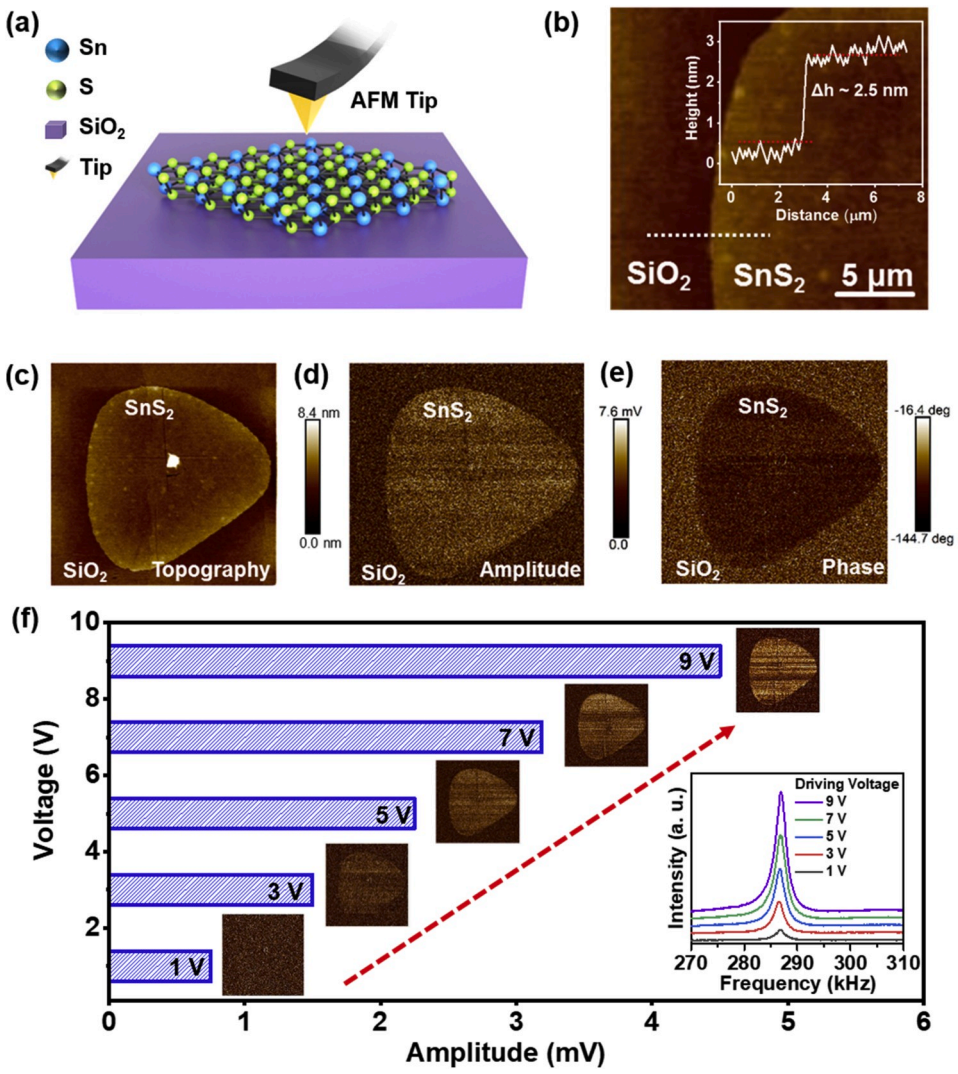

Fig. 2. (a) A schematic illustration represents the PFM measurements of the as-grown SnS_2 NSs on a SiO_2/Si substrate, where an external voltage is applied *via* the AFM tip. (b) The thickness of the tested SnS_2 NSs along the white dashed line is determined to be ~2.5 nm. The measured (c) surface topograph, (d) output amplitude image, and (e) output phase image of the SnS_2 NSs are presented. (f) The gradient of the amplitude images, observed by PFM with the applied tip voltages of 1–9 V, reveals the remarkable inverse piezoelectricity of the SnS_2 NSs. Shown in the inset are the PFM intensities at resonant frequency with different applied voltages.

Table S1 of the Supporting Information, the determined d_{33} value of SnS_2 NSs is superior to those of the TMDCs listed. Moreover, by treating the cantilever-sample system as a damped harmonic oscillator, the measured PFM intensities at resonant frequency (shown in the inset of Fig. 2f) exhibit a linear relation with the applied excitation voltage, further confirming the linear piezoelectricity of SnS_2 NSs [41].

A PENG device with the self-powered and active sensing capabilities has recently shown great impact on the future technologies of energy harvesting, wireless transmission, human-machine interface, and smart healthcare [42]. In this study, we present a prototype flexible SnS_2 PENG (as presented in Fig. 3a–b), for the first time, of which the device contains a conducting channel of 2–5 nm-thick SnS_2 NSs connected electrically by a set of Cr/Au electrodes (with the device fabrications described in Experimental Section and a photo to emphasize the central area of a SnS_2 PENG device shown in Fig. S6).

The output performance of the as-fabricated SnS_2 PENG was investigated systematically by integrating this device into a motor system to receive mechanically controllable sinusoidal strains (as illustrated in Fig. S7). In Fig. 3c−d, the open-circuit voltage (V_{oc}) and short-circuit current (I_{sc}) characteristics of the SnS_2 PENG were measured under a series of sinusoidal excitations, where the typical output responses of $V_{oc} = 6$ mV and $I_{sc} = 60$ pA were obtained.

Shown in Fig. S8 are the compressing and releasing deformations of a SnS_2 PENG, in which the whole process can be divided into three steps. In the initial state (Figs. S8a–I), there is no piezoelectric potential between the two Cr/Au electrodes and no electrical signal is observed. When the PENG is stressed (Fig. S8a-II), a tensile strain is loaded on the SnS_2 PENG to create a dipole moment along the strain direction and generate a piezoelectric potential between the Cr/Au electrodes, resulting in a positive current peak. After the PENG is released (Fig. S8a-III), the tensile strain on the SnS_2 PENG decreases and the piezoelectric potential drops, leading to a negative current peak. The polarity-switching tests shown in Fig. S8b are in accordance with the proposed charge generation process illustrated in Fig. S8a and confirm that the measured output signals are not artifacts. In addition, no output signals could be detected for a PENG device without the channel material of SnS_2 NSs (Fig. S9).

To evaluate the effect of an applied strain on the as-fabricated SnS_2 PENG device, the piezoelectric responses of a SnS_2 PENG were measured under various strain conditions with the strain of ϵ (%) defined in Fig. S10. As shown in Fig. 3e, the typical output peak voltage and current of a SnS_2 PENG can reach 33 mV and 180 pA, respectively, under an external strain of $\epsilon = 0.6\%$. It is noted that the piezoelectric output performance (i.e., the piezoelectric response per unit strain) of a PENG device reflects its strain sensitivity. Fig. S11 summarizes a comparison of the piezoelectric output performance among various 2D materials-fabricated PENG devices, in which the SnS_2 PENG of this work exhibits excellent piezoelectric responses in both current and voltage. To quantify the power output of a SnS_2 PENG, Fig. 3f displays the piezoelectric outputs as a function of external load resistance under the strain

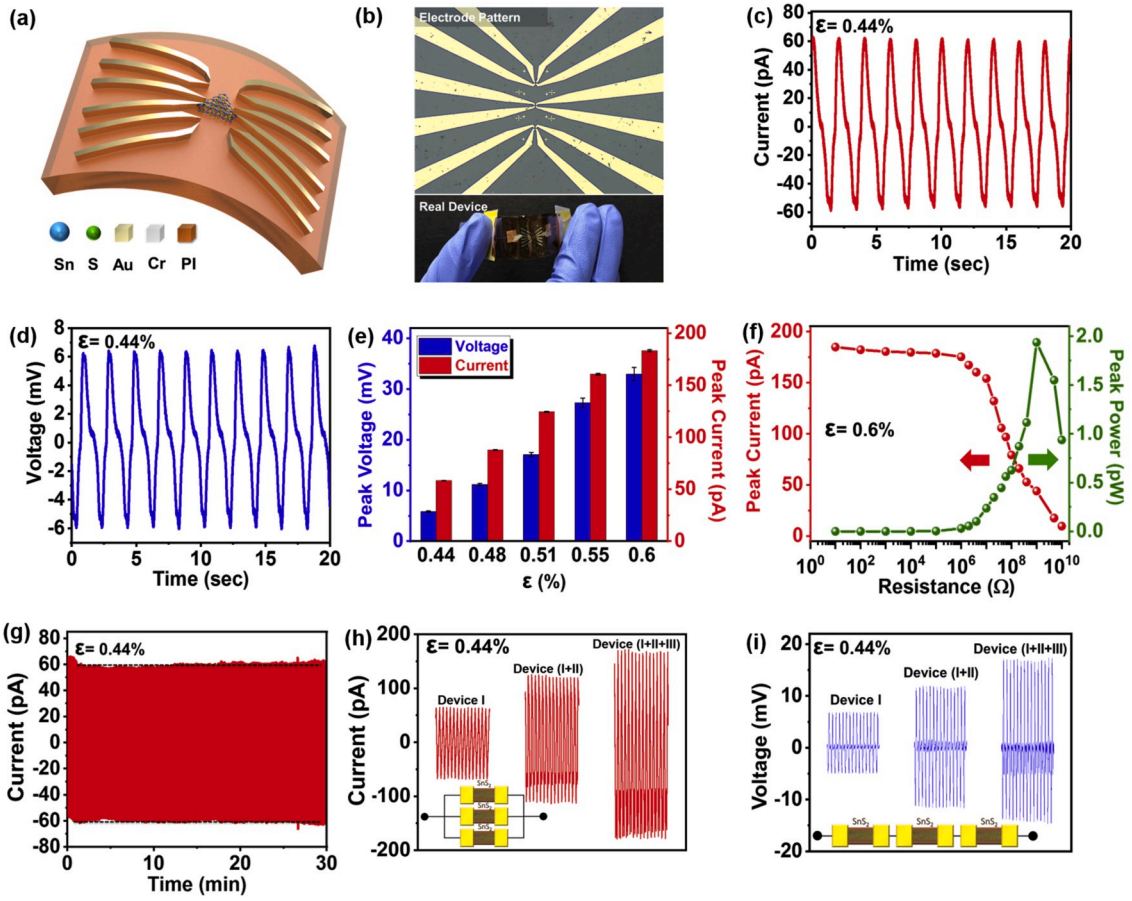

Fig. 3. (a) A schematic illustration represents the as-fabricated SnS_2 PENG device, composed of a SnS_2 channel connected electrically by Cr/Au electrodes on a polyimide substrate. The blue and green spheres represent the Sn and S atoms, respectively. (b) The optical image of a SnS_2 PENG device fabricated by photolithography and a photo of the as-fabricated SnS_2 PENG device. (c–d) The piezoelectric responses of a SnS_2 PENG device under a periodic strain of $\epsilon = 0.44\%$ include the outputs of (c) short circuit current and (d) open circuit voltage. (e) The piezoelectric output responses of a SnS_2 PENG device are plotted as a function of strain (ϵ). The data presented are the mean ± the standard deviation from 20 technical replicates. (f) The peak current and power outputs of a SnS_2 PENG device were measured with different external load resistances under the strain of 0.6%. (g) The device reliability of a SnS_2 PENG device was tested by cyclic output current measurements. (h–i) The constructive output (h) currents and (i) voltages from the linear superposition of individual PENG devices in the parallel and serial connections, respectively, were examined under the strain of 0.44%.

of 0.6%. While the output current shows only small fluctuations for the load resistance of <1 MΩ but decreases drastically at >1 MΩ, the maximum instantaneous power can reach 2 pW at the load resistance of 1 GΩ. The output voltage as a function of load resistance was also investigated in Fig. S12. Notably, the output current (Fig. 3g) and voltage (Fig. S13) of the SnS_2 PENG under the strain of 0.44% remain stable for >30 min (~1000 cycles) without any degradation. Furthermore, diverse applications can be extended by integrating several SnS_2 PENG devices to enhance their output performances. For this demonstration, three SnS_2 PENG devices were selected to make parallel (Fig. 3h) and serial (Fig. 3i) circuit connections (as illustrated in the insets) under the strain of 0.44%, where the peak current and voltage generated by these connections show the proportional enhancements. It is noted that the output performances of a PENG device can be enhanced by optimizing the frequency of applied strain [43]. To better understand the effect of operation frequency on the output performances of a SnS_2 PENG, we performed the calculations with a finite element method (FEM) using COMSOL Multiphysics software. Shown in Fig. S14 are the simulation results, revealing that while the output current increases linearly with increasing applied frequency, the output voltage keeps almost constant. Additionally, we measured the frequency-dependent output performance of our SnS_2 PENG device under various operation frequencies from 0.25 to 2 Hz. As compared in Fig. S14, our experimental results of a SnS_2 PENG agree well with the trends calculated by FEM simulation and are consistent with the previous experimental measurements of a PbI_2 nanosheets-based PENG device [44]. These results open up new possibilities for 2D materials-based PENG devices to be used for nanoscale powering systems, strain sensing technology, and human-machine interface.

For a human-machine interaction (HMI) system, robots play a key role because of their capabilities of mimicking and following out human's motions with even more powerful or precise reinforcement in certain critical situations [45–49]. In the human-robot development, how to manipulate robotic actions to be commensurate with human instruction is critical. It is desirable to establish the human-robot interface in a natural, precise, and interactive manner, for which atomically thin 2D materials-based sensors with a lighter, wireless, powerless, and sensitive design are promising candidates to fulfill this requirement [50–52]. In this work, we demonstrate that a SnS_2 PENG with its strain sensing and self-powered functionalities can be used as a human-robot interaction platform to synchronize human-robot motions. Fig. 4a shows the homemade human-machine interface platform of a fully three-dimension (3D) printed robotic hand in conjunction with an assistive control program. Compared with traditional metal robots, the

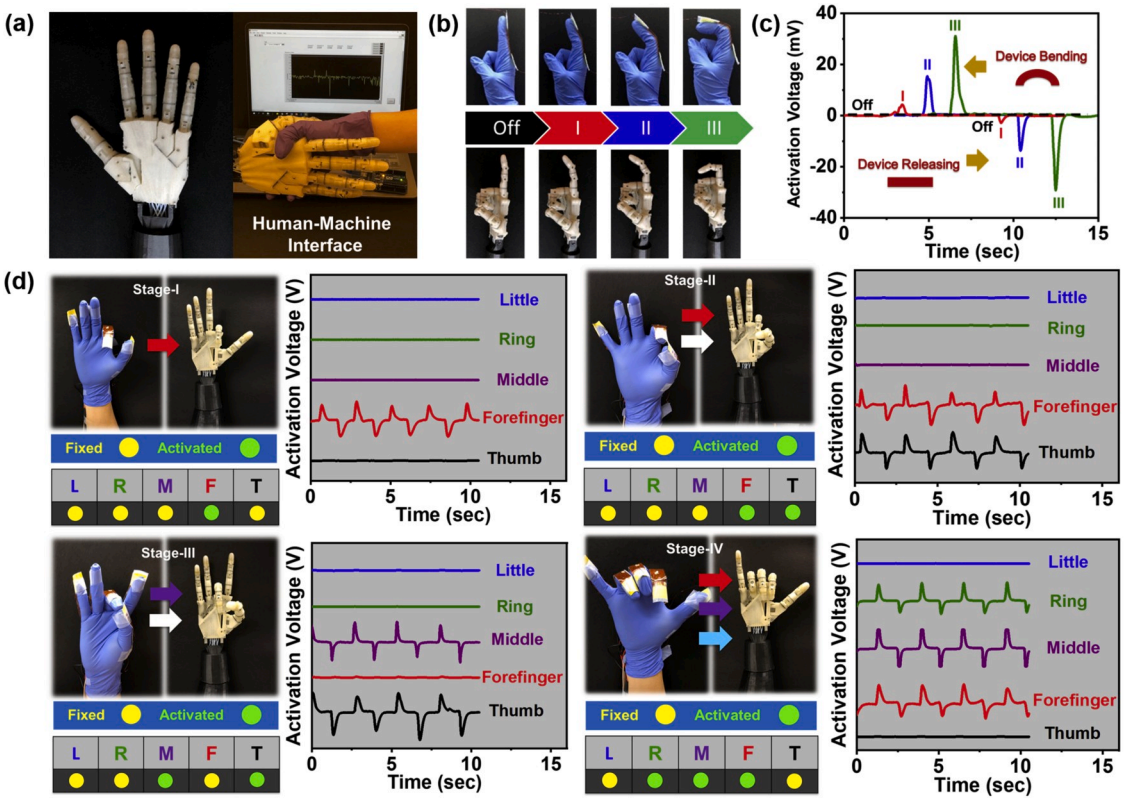

Fig. 4. (a) An intelligent human-robotic interface is established based on the interaction between human and 3D printing robotic hands. (b) The snapshot photos of a human forefinger in different bending states (from the off, I, II, to III states) with (c) the corresponding activation voltages generated synchronously by the SnS_2 PENG device, adhered to the human forefinger, to drive a robotic forefinger. (d) The real-time human-robot imitation is demonstrated by the smart sign language platform of a multi-channel data collecting system. The voltage generated by each bending knuckle is presented for different finger configurations from Stage-I to IV. The yellow and green circles represent the fixed and activated states of the robotic hand, respectively.

3D printed robotic system holds the advantages of creating components in a layer-by-layer manner and offering various options for feature details, structural flexibility, shape adaptability, and multi-functionality toward real applications.

The as-fabricated SnS_2 PENG devices are advantageous for building up a synchronous human-robot control system. Flexible SnS_2 PENG devices can readily adhere to human fingers. When fingers bend and stretch, the adhered SnS_2 PENGs produce signals accordingly, as demonstrated in Fig. S15. The output signals generated by the SnS_2 PENGs can simultaneously be used to drive a robotic hand through the series of signal generation, processing, and recognition (Fig. S16). In Fig. 4b–c, the distinctive activation voltages created by a human forefinger in different bending states (off, I, II, and III) were used concurrently to control the same movements of a robotic forefinger, indicating the successful real-time imitation of human gesture. The finger motions at different bending degrees and their corresponding robotic finger gestures were also demonstrated in Video S17 of the Supporting Information.

Supplementary video related to this article can be found at https://doi.org/10.1016/j.nanoen.2020.104879

To further apply the human-robotic interactive platform for a future HMI system, the real-time performance of a smart sign language system is demonstrated. In Fig. 4d, a wired glove assembled with multiple SnS_2 PENGs by decorating each knuckle with a PENG device was used to harvest human motion for triggering the robotic imitation. Fig. 4d (Stages I to IV) shows the multi-channel signals extracted from the real-time piezoelectric responses to different finger configurations. As can be seen, diverse human-hand gesture can be copied successfully *via* the as-designed human-robot interactive platform, for which a video recording of the real-time human-robot imitation is shown in Video S18 of the Supporting Information.

Supplementary video related to this article can be found at https://doi.org/10.1016/j.nanoen.2020.104879

Furthermore, advanced robotic sensors are essential for developing the artificial skin, gesture interpretation, and haptic sensing systems. In this study, we also demonstrate that a set of SnS_2 PENGs can be utilized as strain sensing units in the human-robot interface to directly translate the robotic gesture into electrical outputs. In Fig. S19, we mounted five SnS_2 PENGs on the joints of five robotic fingers, where each robotic finger represents a specific number from "0" to "4", corresponding to the thumb (T), forefinger (F), middle finger (M), ring finger (R), and little finger (L). Before mounting on the robotic hands, five SnS_2 PENGs were tested to confirm that their output performances are similar under the strain of 0.44% (Fig. S20). We defined that the initial state of the robotic hand is in the full expansion of five fingers and the output signals of the deformed strain sensing array on the robotic fingers can build up a smart language system. These results demonstrate that 2D materials-based PENG devices have great potential for not only harvesting biomechanical energy to activate an advanced human-robotic interactive system, but also well-suited for enabling sensing applications in future HMI system.

4. Conclusion

In summary, the intrinsic piezoelectricity of the CVD-grown SnS_2 NSs was studied for the first time. The prominent inverse piezoelectricity of SnS_2 NSs was investigated by PFM. The as-synthesized SnS_2 NSs were further fabricated to be a PENG device to transform ambient mechanical

energy into electricity. The typical output performance of the as-fabricated SnS_2 PENG device can reach the open-circuit voltage and short-circuit current of 6 mV and 60 pA, respectively. The maximum instantaneous power of the SnS_2 PENG can achieve 2 pW under the strain of 0.6%. Moreover, with the robust energy harvesting and self-powered capabilities, the SnS_2 PENG devices can be used as a drive unit of the synchronous human-robot interface for an advanced smart sign language system. These findings not only advance 2D materials-based devices toward multi-functional biomechanical harvesters, but also open up an avenue to develop enabling sensing technology and human-machine interface in the near future.

Declaration of competing interest

The authors declare that they have no known competing financial interests or personal relationships that could have appeared to influence the work reported in this paper.

CRediT authorship contribution statement

Po-Kang Yang: Conceptualization, Methodology, Validation, Investigation, Resources, Writing - original draft, Writing - review & editing, Visualization, Project administration, Funding acquisition. **Sui-An Chou:** Conceptualization, Methodology, Validation, Investigation, Writing - review & editing, Visualization. **Ching-Hung Hsu:** Methodology, Software, Formal analysis, Writing - review & editing. **Roshan Jesus Mathew:** Investigation, Validation. **Kuan-Hsuan Chiang:** Investigation, Validation. **Jung-Yen Yang:** Investigation, Validation, Resources. **Yit-Tsong Chen:** Conceptualization, Methodology, Resources, Writing - review & editing, Supervision, Data curation, Visualization, Project administration, Funding acquisition.

Acknowledgements

This work was supported, in part, by the Ministry of Science and Technology (MOST) of Taiwan under Grant nos. 106-2113-M-002-022-MY3 and 107-2113-M-002-011-MY3. P.-K. Yang thanks the support of MOST of Taiwan under Grant no. 108-2636-E-038-003 (Young Scholar Fellowship Program). The assistances of Miss C.-Y. Chien in HR-TEM measurements, Mrs. Y.-T. Lao and Mr. H. Lu in PFM measurements, and Mr. T.-E. Chien and Mr. W.-X. Liu in the early course of experiments are greatly acknowledged.

Appendix A. Supplementary data

Supplementary data to this article can be found online at https://doi.org/10.1016/j.nanoen.2020.104879.

References

[1] K.S. Novoselov, A.K. Geim, S.V. Morozov, D. Jiang, Y. Zhang, S.V. Dubonos, I. V. Grigorieva, A.A. Firsov, Science 306 (2004) 666–669.
[2] S. Stankovich, D.A. Dikin, G.H.B. Dommett, K.M. Kohlhaas, E.J. Zimney, E. A. Stach, R.D. Piner, S.B.T. Nguyen, R.S. Ruoff, Nature 442 (2006) 282–286.
[3] B. Radisavljevic, A. Radenovic, J. Brivio, V. Giacometti, A. Kis, Nat. Nanotechnol. 6 (2011) 147–150.
[4] H. Zeng, J. Dai, W. Yao, D. Xiao, X. Cui, Nat. Nanotechnol. 7 (2012) 490–493.
[5] S. Bertolazzi, J. Brivio, A. Kis, ACS Nano 5 (2011) 9703–9709.
[6] Y. Wang, N. Xu, D. Li, J. Zhu, Adv. Funct. Mater. 27 (2017) 1604134.
[7] M. Chhowalla, H.S. Shin, G. Eda, L.J. Li, K.P. Loh, H. Zhang, Nat. Chem. 5 (2013) 263–275.
[8] C. Cui, F. Xue, W.J. Hu, L.J. Li, npj 2D Mater, Appl 2 (2018) 18.
[9] J. Qi, Y.W. Lan, A.Z. Stieg, J.H. Chen, Y.L. Zhong, L.J. Li, C.D. Chen, Y. Zhang, K. L. Wang, Nat. Commun. 6 (2015) 7430.
[10] M.N. Blonsky, H.L. Zhuang, A.K. Singh, R.G. Hennig, ACS Nano 9 (2015) 9885–9891.
[11] W. Wu, L. Wang, Y. Li, F. Zhang, L. Lin, S. Niu, D. Chenet, X. Zhang, Y. Hao, T. F. Heinz, J. Hone, Z.L. Wang, Nature 514 (2014) 470–474.
[12] S.A. Han, T.H. Kim, S.K. Kim, K.H. Lee, H.J. Park, J.H. Lee, S.W. Kim, Adv. Mater. 30 (2018) 1800342.
[13] J. Yu, J. Li, W. Zhang, H. Chang, Chem. Sci. 6 (2015) 6705–6716.
[14] F. Xue, J. Zhang, W. Hu, W.T. Hsu, A. Han, S.F. Leung, J.K. Huang, Y. Wan, S. Liu, J. Zhang, J.H. He, W.H. Chang, Z.L. Wang, X. Zhang, L.J. Li, ACS Nano 12 (2018) 4976–4983.
[15] M.M. Alyörük, Y. Aierken, D. Çaklr, F.M. Peeters, C. Sevik, J. Phys. Chem. C 119 (2015) 23231–23237.
[16] X. Jia, C. Tang, R. Pan, Y. Long, C. Gu, J. Li, ACS Appl. Mater. Interfaces 10 (2018) 18073–18081.
[17] B. Li, T. Xing, M. Zhong, L. Huang, N. Lei, J. Zhang, J. Li, Z. Wei, Nat. Commun. 8 (2017) 1958.
[18] I. Shown, S. Samireddi, Y.C. Chang, R. Putikam, P.H. Chang, A. Sabbah, F.Y. Fu, W. F. Chen, C.I. Wu, T.Y. Yu, P.W. Chung, M.C. Lin, L.C. Chen, K.H. Chen, Nat. Commun. 9 (2018) 169.
[19] H. Yang, J.H. Bahk, T. Day, A.M.S. Mohammed, G.J. Snyder, A. Shakouri, Y. Wu, Nano Lett. 15 (2015) 1349–1355.
[20] X. Zhang, Y. Cui, L. Sun, M. Li, J. Du, Y. Huang, J. Mater. Chem. C 7 (2019) 13203–13210.
[21] Y. Huang, E. Sutter, J.T. Sadowski, M. Cotlet, O.L.A. Monti, D.A. Racke, M. R. Neupane, D. Wickramaratne, R.K. Lake, B.A. Parkinson, P. Sutter, ACS Nano 8 (2014) 10743–10755.
[22] J.H. Ahn, M.J. Lee, H. Heo, J.H. Sung, K. Kim, H. Hwang, M.H. Jo, Nano Lett. 15 (2015) 3703–3708.
[23] G. Su, V.G. Hadjiev, P.E. Loya, J. Zhang, S. Lei, S. Maharjan, P. Dong, P.M. Ajayan, J. Lou, H. Peng, Nano Lett. 15 (2015) 506–513.
[24] L.A. Burton, T.J. Whittles, D. Hesp, W.M. Linhart, J.M. Skelton, B. Hou, R. F. Webster, G. O'Dowd, C. Reece, D. Cherns, D.J. Fermin, T.D. Veal, V.R. Dhanak, A. Walsh, J. Mater. Chem. 4 (2016) 1312–1318.
[25] X. Zhou, Q. Zhang, L. Gan, H. Li, T. Zhai, Adv. Funct. Mater. 26 (2016) 4405–4413.
[26] Z. Zhang, C. Shao, X. Li, Y. Sun, M. Zhang, J. Mu, P. Zhang, Z. Guo, Y. Liu, Nanoscale 5 (2013) 606–618.
[27] G. Liu, Y. Qiu, Z. Wang, J. Zhang, X. Chen, M. Dai, D. Jia, Y. Zhou, Z. Li, P. Hu, ACS Appl. Mater. Interfaces 9 (2017) 37750–37759.
[28] X. Chia, P. Lazar, Z. Sofer, J. Luxa, M. Pumera, J. Phys. Chem. C 120 (2016) 24098–24111.
[29] J.A. Christman, R.R. Woolcott, A.I. Kingon, R.J. Nemanich, Appl. Phys. Lett. 73 (1998) 3851–3853.
[30] X. Wang, X. He, H. Zhu, L. Sun, W. Fu, X. Wang, L.C. Hoong, H. Wang, Q. Zeng, W. Zhao, J. Wei, Z. Jin, Z. Shen, J. Liu, T. Zhang, Z. Liu, Sci. Adv. 2 (2016), e1600209.
[31] S.K. Kim, R. Bhatia, T.H. Kim, D. Seol, J.H. Kim, H. Kim, W. Seung, Y. Kim, Y. H. Lee, S.W. Kim, Nano Energy 22 (2016) 483–489.
[32] C.J. Brennan, R. Ghosh, K. Koul, S.K. Banerjee, N. Lu, E.T. Yu, Nano Lett. 17 (2017) 5464–5471.
[33] J. Zhang, L. Song, M. Sist, K. Tolborg, B.B. Iversen, Nat. Commun. 9 (2018) 4716.
[34] J.M. Gonzalez, I.I. Oleynik, Phys. Rev. B Condens. Matter 94 (2016) 125443.
[35] A. Kuhn, T. Holzmann, J. Nuss, B.V. Lotsch, J. Mater. Chem. 2 (2014) 6100–6106.
[36] M. de Jong, W. Chen, H. Geerlings, M. Asta, K.A. Persson, Sci. Data 2 (2015) 150053.
[37] A. Safari, E.K. Akdoğan, Piezoelectric Acoust. Mater. Transducer Appl. (2008) 17–38.
[38] S. Yuan, X. Luo, H.L. Chan, C. Xiao, Y. Dai, M. Xie, J. Hao, Nat. Commun. 10 (2019) 1775.
[39] Y. Zhou, D. Wu, Y. Zhu, Y. Cho, Q. He, X. Yang, K. Herrera, Z. Chu, Y. Han, M. C. Downer, H. Peng, K. Lai, Nano Lett. 17 (2017) 5508–5513.
[40] S. Kang, S. Kim, S. Jeon, W.S. Jang, D. Seol, Y.M. Kim, J. Lee, H. Yang, Y. Kim, Nano Energy 58 (2019) 57–62.
[41] M. Zelisko, Y. Hanlumyuang, S. Yang, Y. Liu, C. Lei, J. Li, P.M. Ajayan, P. Sharma, Nat. Commun. 5 (2014) 4284.
[42] Q. Zheng, B. Shi, Z. Li, Z.L. Wang, Adv. Sci. 4 (2017) 1700029.
[43] L. Xing, Y. Nie, X. Xue, Y. Zhang, Nano Energy 10 (2014) 44–52.
[44] H. Song, I. Karakurt, M. Wei, N. Liu, Y. Chu, J. Zhong, Nano Energy 49 (2018) 7–13.
[45] X. Pu, H. Guo, Q. Tang, J. Chen, L.S. Feng, G. Liu, X. Wang, Y. Xi, C. Hu, Z.L. Wang, Nano Energy 54 (2018) 453–460.
[46] J. Byun, Y. Lee, J. Yoon, B. Lee, E. Oh, S. Chung, T. Lee, K.J. Cho, J. Kim, Y. Hong, Sci. Robot 3 (2018), eaas9020.
[47] J.C. Yeo, H.K. Yap, W. Xi, Z. Wang, C.H. Yeow, C.T. Lim, Adv. Mater. Technol. 1 (2016) 1600018.
[48] X. Pu, H. Guo, J. Chen, X. Wang, Y. Xi, C. Hu, Z.L. Wang, Sci. Adv. 3 (2017), e1700694.
[49] H. Guo, X. Pu, J. Chen, Y. Meng, M.-H. Yeh, G. Liu, Q. Tang, B. Chen, D. Liu, S. Qi, C. Wu, C. Hu, J. Wang, Z.L. Wang, Sci. Robot. 3 (2018) eaat2516.
[50] Y. Wang, L. Wang, T. Yang, X. Li, X. Zang, M. Zhu, K. Wang, D. Wu, H. Zhu, Adv. Funct. Mater. 24 (2014) 4666–4670.
[51] M.G. Campbell, S.F. Liu, T.M. Swager, M. Dincə, J. Am. Chem. Soc. 137 (2015) 13780–13783.
[52] M. Donarelli, S. Prezioso, F. Perrozzi, F. Bisti, M. Nardone, L. Giancaterini, C. Cantalini, L. Ottaviano, Sensor. Actuator. B Chem. 207 (2015) 602–613.

Dr. Po-Kang Yang received his Ph.D. degree from Graduate Institute of Photonics and Optoelectronics, National Taiwan University. He is currently an assistant professor in Graduate Institute of Nanomedicine and Medical Engineering, College of Biomedical Engineering, Taipei Medical University. His research interests include the development of nanomaterials, energy harvesting, self-powered nanosystems, and biomedical electronics.

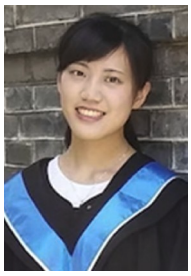

Sui-An Chou is currently a M.S. student under the supervision of Prof. Yit-Tsong Chen in Department of Chemistry, National Taiwan University. She received her Bachelor's degree in Applied Chemistry from National Chiao Tung University. Her present research interests mainly focus on the synthesis of advanced two-dimensional materials and the development of flexible self-powered systems for further artificial intelligent applications.

Ching-Hung Hsu is currently a research assistant in Department of Chemistry, National Taiwan University. He received his M.S. degree from Institute of Biomedical Engineering from National Chiao Tung University. His major research interests include design and fabrication of nanoelectronic sensors, field-effect transistor-based biosensors, and the development of human-machine interactive platforms.

Roshan Jesus Mathew obtained his M.Phil. degree in Nano Science and Technology from Bharathiar University, India. He is now pursuing his Ph.D. degree in Engineering & System Sciences at National Tsing Hua University in collaboration with the TIGP Nano Science & Technology Program at Academia Sinica, Taiwan. His research interests are focused on the themes of 2D materials, such as to synthesize novel 2D materials and to explore the optical, electronic, and structural properties of 2D materials-based devices for nano electronics and energy applications.

Kuan-Hsuan Chiang received his M.S. degree from Institute of Chemistry, National Cheng Kung University. He is a research assistant at Dr. Yit-Tsong Chen's lab in National Taiwan University. His research interests include the synthesis of single-crystal metal chalcogenides, characterization of crystal compositions, and analysis of crystal structures.

Dr. Jung-Yen Yang received his Ph.D. degree from the Institute of Chemistry, National Taiwan University. He is currently an associate researcher in the Materials Analysis Division, Taiwan Semiconductor Research Institute. His research interests include the fluorescent nanomaterials synthesis, compositional and structural characterizations for thin films, and portable analytical techniques.

Dr. Yit-Tsong Chen is a professor in Department of Chemistry at National Taiwan University. He is also an adjunct Research Fellow at Institute of Atomic and Molecular Sciences, Academia Sinica in Taiwan. He received his B.S. degree from National Taiwan University, Ph.D. degree from University of Chicago, and postdoctoral research training at MIT. His current interests are focused on (i) applying nanoscale field-effect transistor biosensors to study protein-protein interaction, extracellular ionic fluctuation, cellular exo-endocytosis, and neuron-neuron interaction and (ii) catalytic synthesis and architectural design of one- and two-dimensional nanomaterials on multiple functional devices for optoelectronic, energy conversion/storage, and biosensing applications.

Supporting Information

Tin Disulfide Piezoelectric Nanogenerators for Biomechanical Energy Harvesting and Intelligent Human-Robot Interface Applications

Po-Kang Yang[a,e], Sui-An Chou[b,c], Ching-Hung Hsu[b,c], Roshan Jesus Mathew[b,c,f,g], Kuan-Hsuan Chiang[b,c], Jung-Yen Yang[d], and Yit-Tsong Chen[b,c,*]

[a] Graduate Institute of Nanomedicine and Medical Engineering, College of Biomedical Engineering, Taipei Medical University, Taipei 11031, Taiwan.

[b] Department of Chemistry, National Taiwan University, No. 1, Sec. 4, Roosevelt Road, Taipei 106, Taiwan.

[c] Institute of Atomic and Molecular Sciences, Academia Sinica, P.O. Box 23-166, Taipei 106, Taiwan.

[d] National Applied Research Laboratories, Taiwan Semiconductor Research Institute, No. 26, Prosperity Road I, Hsinchu 30078, Taiwan.

[e] International Ph.D. Program in Biomedical Engineering, College of Biomedical Engineering, Taipei Medical University, Taipei 11031, Taiwan.

[f] Department of Engineering and System Science, National Tsing Hua University, Taiwan.

[g] Nano-Science and Technology Program, Taiwan International Graduate Program, Academia Sinica, Taiwan.

[*]Corresponding author: ytcchem@ntu.edu.tw

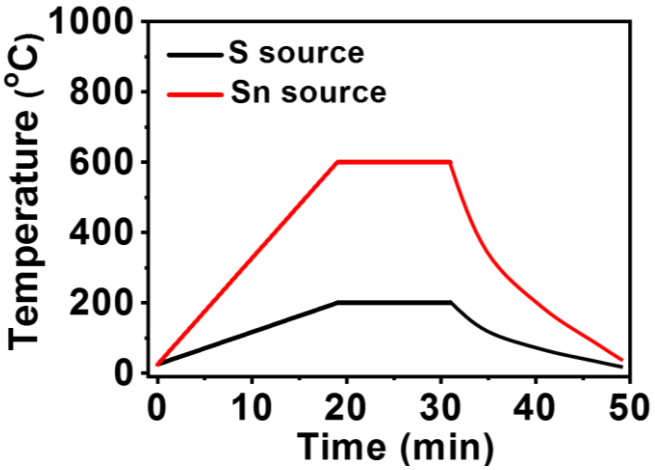

Figure S1. The temporal reaction-temperature profiles for the crystal growth of few-layered SnS_2 NSs in the CVD reactions with SnC_2O_4 and S as chemical precursors.

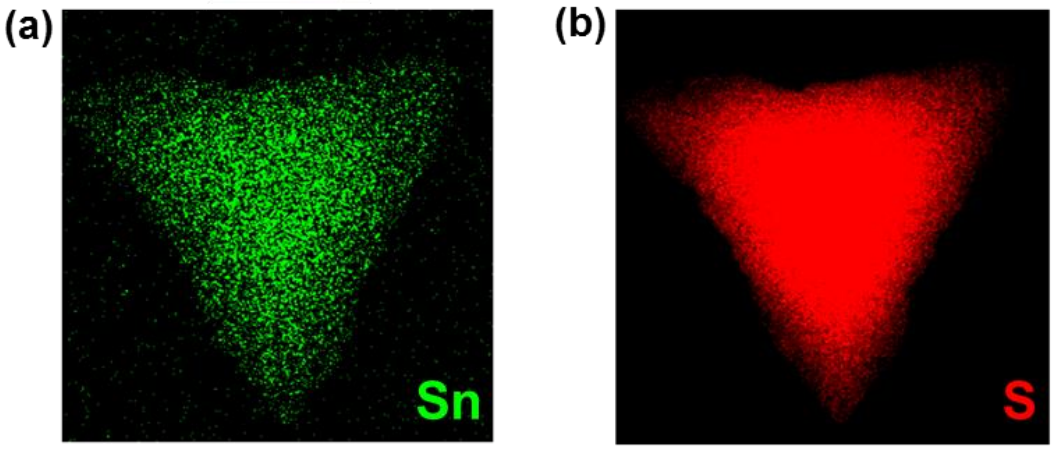

Figure S2. (a–b) EDX mappings of the Sn and S elements distributed in the as-synthesized SnS_2 NSs.

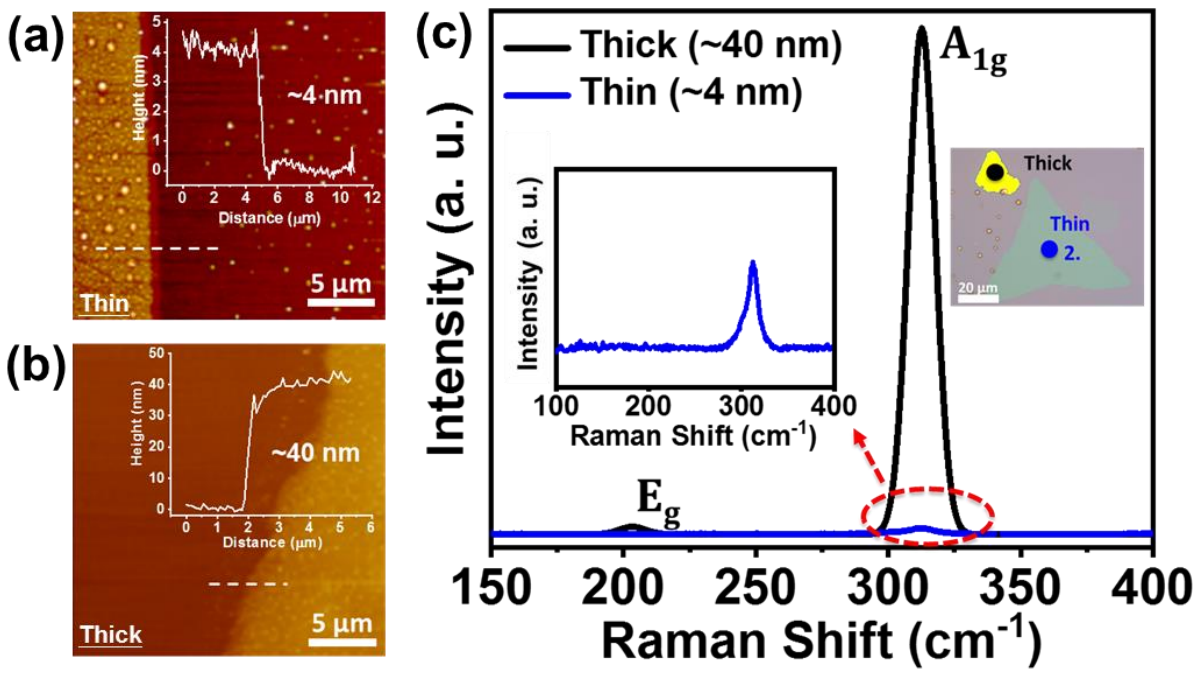

Figure S3. (a–b) The surface topographs of two CVD-grown SnS_2 NSs, with their morphologies shown in the right-hand side inset of (c) and denoted by thin and thick layers, were scanned by AFM to determine their thicknesses of (a) ~4 nm for the thin layer and (b) ~40 nm for the thick layer. (c) Raman spectra of the thin (blue trace) and thick (black trace) SnS_2 NSs were observed with the laser excitation at 532 nm. The magnified Raman spectrum of the thin SnS_2 NSs is displayed in the left-hand side inset. The scale bar in the right-hand side inset is 20 μm.

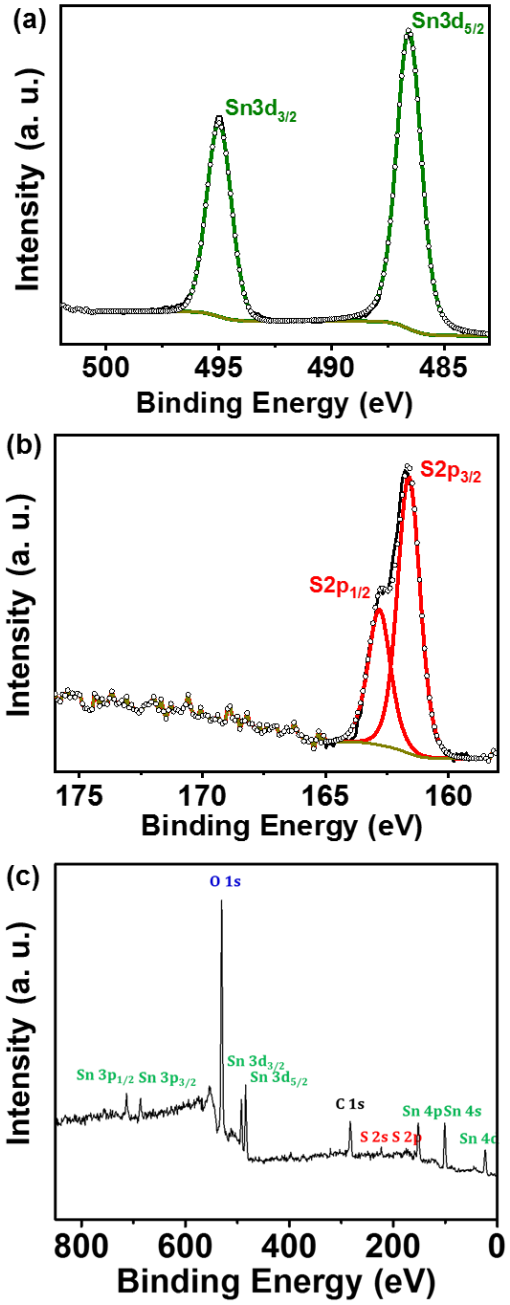

Figure S4. (a–b) XPS spectra of the as-synthesized SnS_2 NSs were observed to analyze the binding energies of the Sn 3d and S 2p levels. (c) A wide-range XPS spectrum of the as-synthesized SnS_2 on a SiO_2/Si substrate includes all elemental constituents, confirming the absence of undesired elements in the synthesized samples. The O 1s peak arises from the oxygen content of the SiO_2/Si substrate and the C 1s peak is attributed to the adventitious carbon.

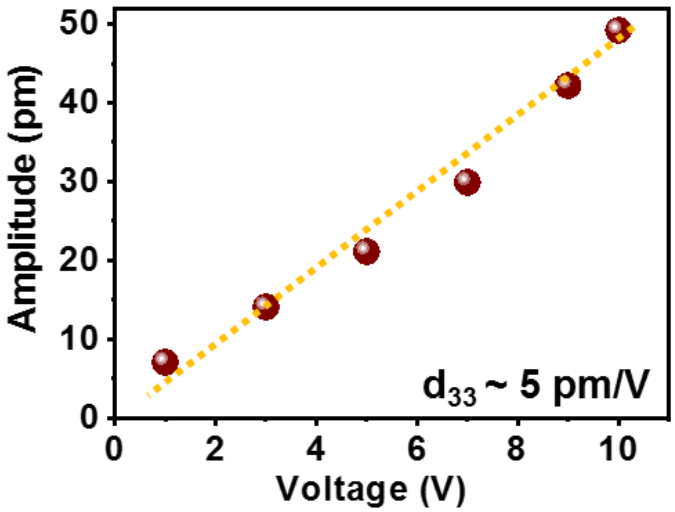

Figure S5. The average amplitude as a function of the applied voltage is plotted with the experimental data points taken from Figure 2f. The piezoelectric coefficient (d_{33}) of SnS_2 NSs is determined to be ~5 pm/V from the linear regression line.

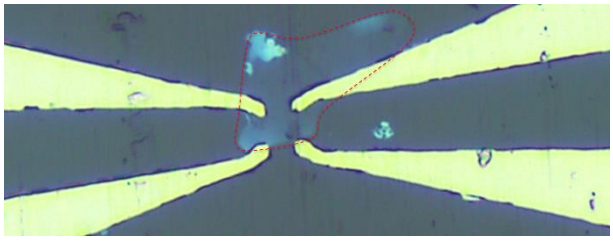

Figure S6. A photo shows the central area of a SnS_2 PENG device, where a SnS_2 NS (demarcated by red dots) is electrically connected by the patterned electrodes fabricated with a standard photolithographic process.

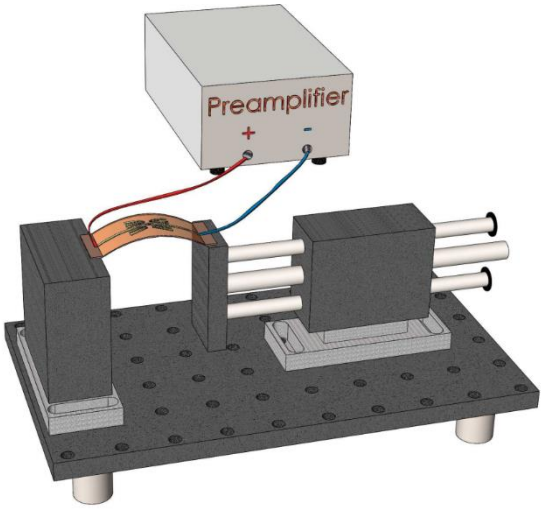

Figure S7. A testing model, containing a commercial motor system, the SnS_2 PENG to be tested, and a preamplifier, was used to characterize the output performance of the SnS_2 PENG device.

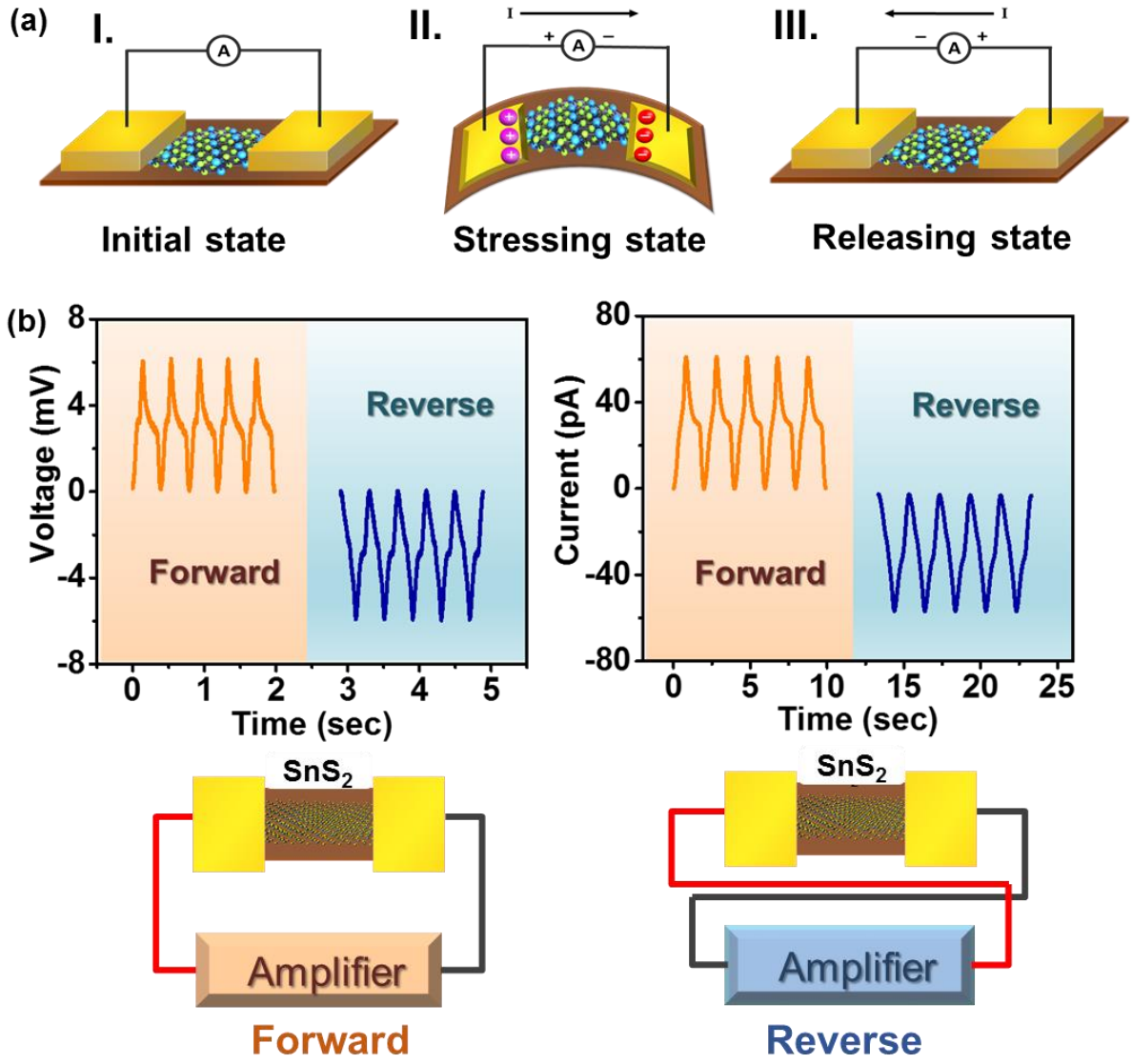

Figure S8. (a) A schematic diagram represents the electricity generation process in a SnS_2 PENG device under the (I) initial, (II) stressing, and (III) releasing states. (b) The switching-polarity (forward and reverse) tests of a SnS_2 PENG device were performed, yielding the voltage and current outputs. The corresponding circuit diagrams of the forward and reverse configurations are also illustrated.

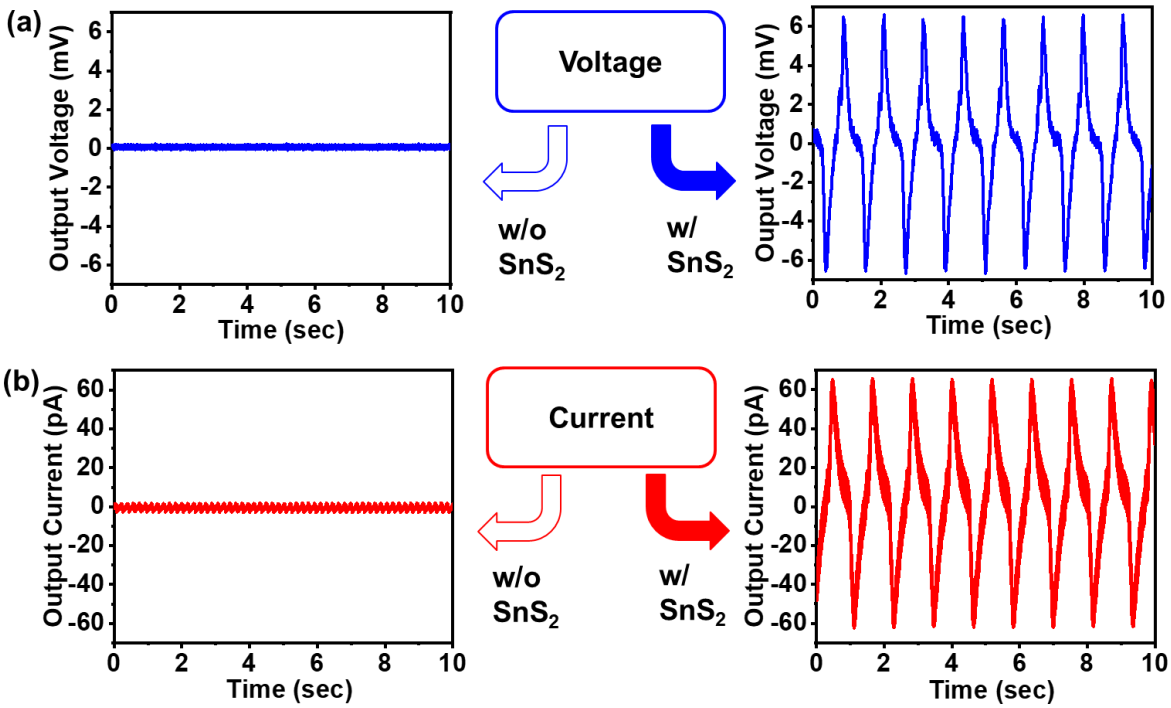

Figure S9. A comparison of the typical electrical outputs of (a) voltage and (b) current for a PENG device with (the right-hand side column) or without (the left-hand side column) the semiconducting channel of SnS_2 NSs.

(a)

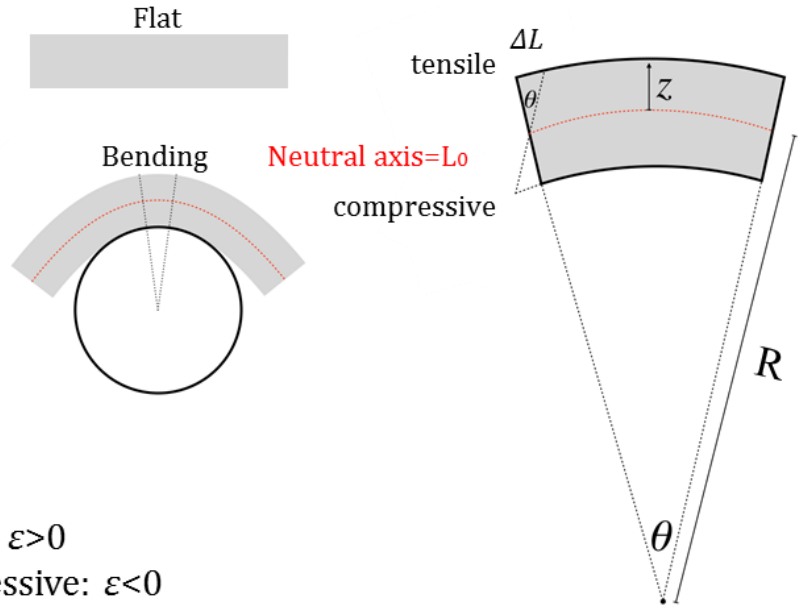

tensile: $\varepsilon>0$

compressive: $\varepsilon<0$

$$\varepsilon\ (\text{strain}) = \frac{\Delta L}{L} = \frac{L'-L}{L} = \frac{(R+Z)*\theta - R*\theta}{R*\theta} = \frac{Z\theta}{R\theta} = \frac{Z}{R}$$

$$\varepsilon\ (\%) = \frac{\Delta L}{L_0} \times 100\%$$

(b)

Distance (mm)	15-25	15-27.5	15-30	15-32.5	15-35
Ɛ (%)	0.44%	0.48%	0.51%	0.55%	0.6%
Sample Photos	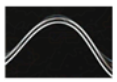	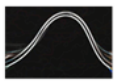	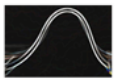	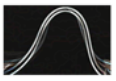	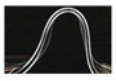

Figure S10. (a) The mechanical strain of ε (%) of a bending device is illustrated and calculated. L_0 is the original length of the channel material in the device. A neutral axis is the position where the channel length remains unchanged during a bending process. ΔL is the change in the channel length after bending. R is the bending radius of the device and Z is the vertical distance from the neutral axis to the outer/inner layer of the channel material. (b) Several values of ε (%) from different bending states of a SnS_2 PENG device are calculated with the corresponding sample photos shown in the bottom panel.

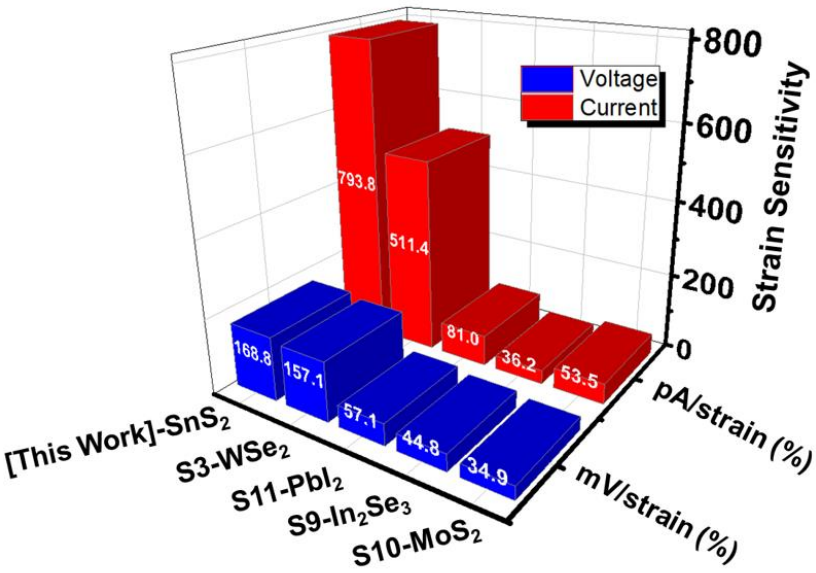

Figure S11. The strain sensitivities of different 2D materials-based PENGs are compared, where the values of the piezoelectric output responses (voltage and current) per unit strain ε (%) are highlighted by white color.

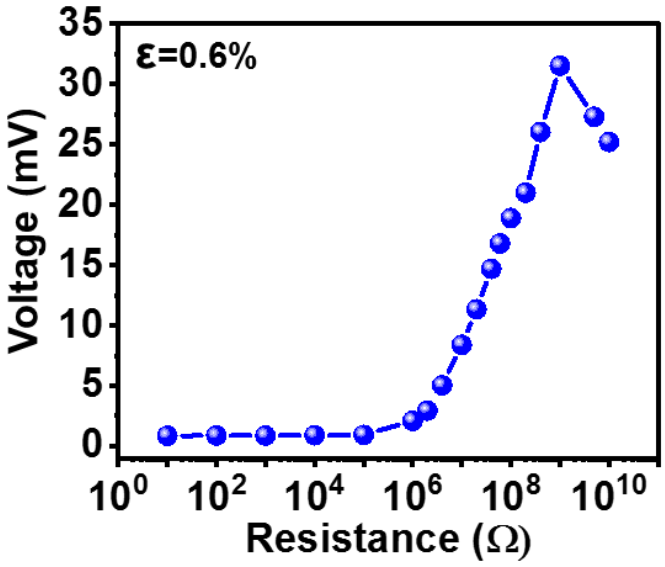

Figure S12. The peak voltage outputs of a SnS_2 PENG device were measured with different external load resistances under the strain of 0.6%.

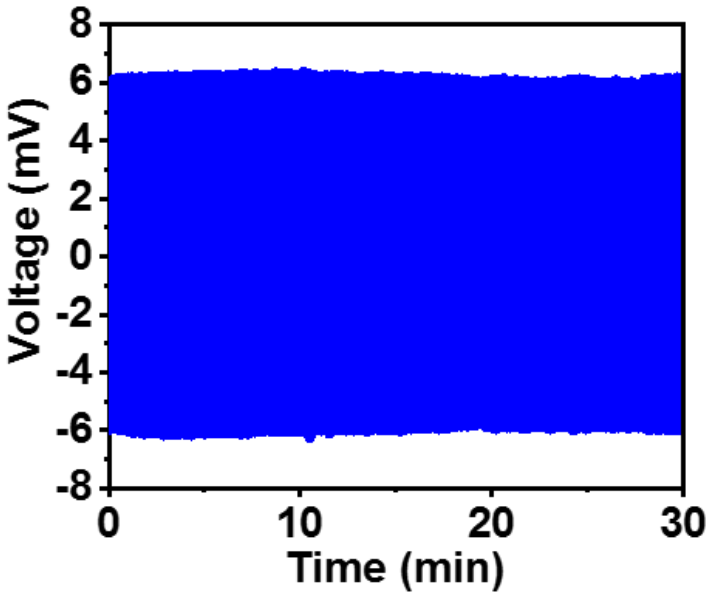

Figure S13. The durability test of a SnS_2 PENG device is demonstrated by measuring its constant output voltage under the strain of 0.44%. The data were collected in ~1000 cycles for 30 min.

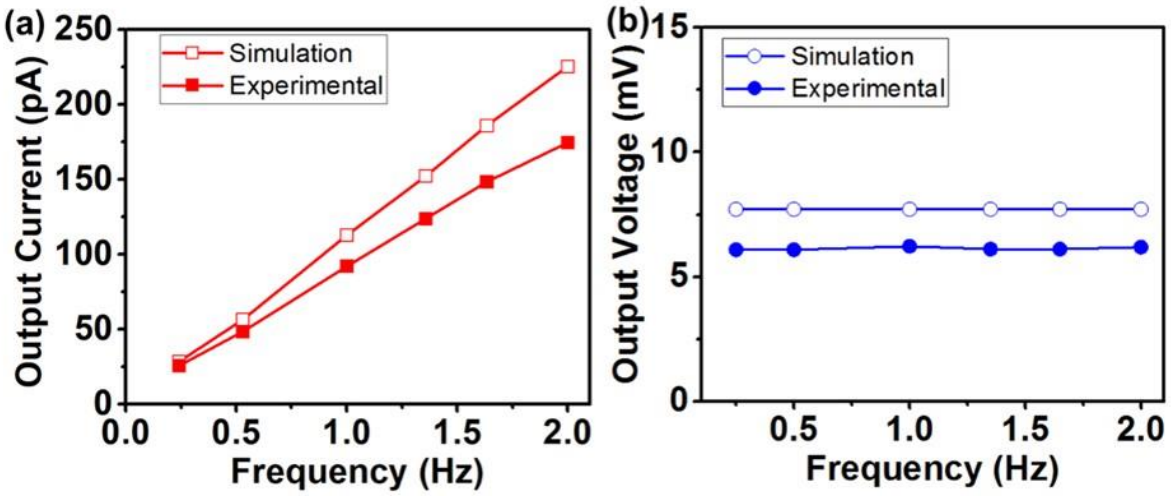

Figure S14. The (a) output currents and (b) output voltages of a SnS_2 PENG device under various operation frequencies were obtained from experimental measurements (solid dots) and FEM simulation (empty dots).

Notes for Figure S14

For the intrinsic piezoelectric properties in a 2D material, the linear piezoelectric effect can be viewed as the first-order coupling of the surface polarization (P_i) (or the macroscopic electric field (E_i)) with the stress (σ_{jk}) and strain (ε_{jk}) tensors, where *i*, *j*, and *k* ($\in$ 1, 2, and 3) correspond to the x, y, and z axes, respectively.[S12,S13] The effect can be described using the third-rank piezoelectric tensor (d_{ijk}), piezoelectric coefficient (e_{ijk}), elastic stiffness coefficient (C_{ijkl}), and their respective Maxwell relations as expressed in equations (1)–(3) below.

$$d_{ijk} = \frac{\partial P_i}{\partial \sigma_{jk}} \quad (1)$$

$$e_{ijk} = \frac{\partial P_i}{\partial \varepsilon_{jk}} \quad (2)$$

$$C_{ijkl} = \frac{\partial \sigma_{ij}}{\partial \varepsilon_{kl}} \quad (3)$$

Moreover, the total number of independent tensor components can be reduced by the crystal symmetry constraints of a 2D crystal system.[S14] Accordingly, e_{ijk} and d_{ijk} can be represented as e_{ij} and d_{ij}, respectively. In addition, the C_{jk} of the elastic stiffness tensor correlates to both e_{ik} and d_{ij} by

$$e_{ik} = d_{ij} C_{jk} \quad (4)$$

In the stress-charge form, the electrical displacement (*D*) can be defined as in equation (5), involving the terms of piezoelectric coefficient tensor (*e*), strain (*S*), electric field (*E*), surface polarization (*P*), and permittivity (ϵ_s), where $\epsilon_s = \epsilon_r \epsilon_0$ and ϵ_0 is the vacuum permittivity with the value of 8.85×10^{-12} F m^{-1}.

$$D = e \cdot S + \epsilon_s \cdot E = P + \epsilon_s \cdot E \quad (5)$$

The electrical displacement (*D*) is the major contribution to the outputs of a PENG device in producing the displacement current (J_D),[S15] which can be presented as

$$J_D = \frac{\partial D}{\partial t} = \epsilon_s \frac{\partial E}{\partial t} + \frac{\partial P}{\partial t} \quad (6)$$

By considering the polarization along the z-axis of a specific material, the relationship between the output characteristics of a PENG device and piezoelectric charges can be expressed as

$$J_D = \frac{\partial P_z}{\partial t} = \frac{\partial \rho_p(z)}{\partial t} \quad (7)$$

$$V_{oc} = z \frac{\rho_p(z)}{\epsilon_s} \quad (8)$$

$$I_{sc} = A \frac{d\rho}{dt} = z\left[\rho_p(z) - \rho(z)\right] / [R \cdot \epsilon_s] \quad (9)$$

In equations (7)–(9), $\rho_p(z)$ represents the piezoelectric polarization charge density on the surface of the material and $\rho(z)$ is the free electron charge density in the electrodes. *R* is an external load and *A* is the area of the device channel. The V_{oc} and I_{sc} represent the output voltage and current, respectively. It should be noted that no external electric field is needed under this circumstance ($E = 0$).

In our model simulation, a force was applied at one end while the other end was assumed to be fixed and electrically grounded. The parameters used in the COMSOL software are: radius $r = 6$ μm and height $h = 4$ nm. The required material parameters of SnS_2 within the matrices are defined as usual and taken from previous reports.[S16,S17] The piezoelectric coefficient tensor (e_{ij}) of SnS_2, belonging to a hexagonal crystal system, has been reported as

$$e_{ij} = \begin{bmatrix} 0 & 0 & 0 & 0 & -0.0142 & 0 \\ 0 & 0 & 0 & -0.01419 & 0 & 0 \\ 0 & 0 & -0.00262 & 0 & 0 & 0 \end{bmatrix}$$

The simulation results of the output currents and voltages of the SnS_2 PENG device used in this study are presented in Figure S14.

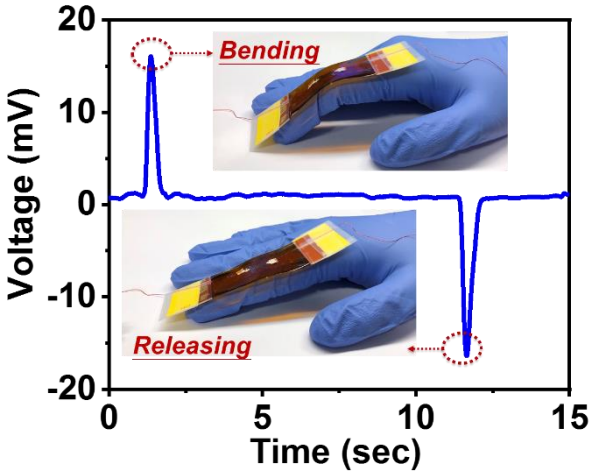

Figure S15. A SnS_2 PENG device adhered to a human forefinger was used to scavenge the mechanical energy induced by the finger's motion.

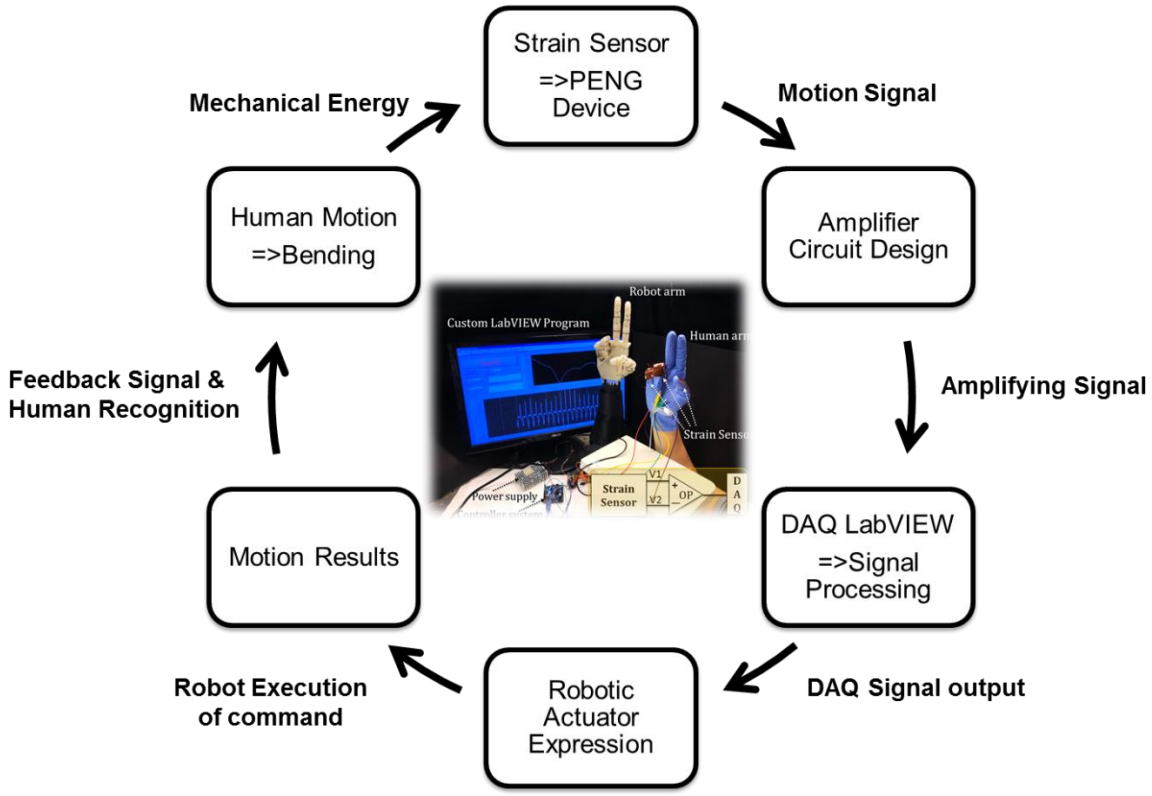

Figure S16. The experimental setup and a flow chart of the system design are presented for the human-machine interface control. A set of SnS_2 PENG devices was incorporated with human fingers as the driving units, which enable robotic arms to mimic human gesture. The synchronous human-robotic motions can be demonstrated by the same acts of both human and robotic fingers according to the stimulation signals generated by the human fingers' motions.

Video S17. A movie file is supplied to demonstrate the finger motions at different bending degrees and their corresponding robotic finger gestures.

Video S18. A movie file is supplied to demonstrate the as-designed human-robot interactive platform, where diverse human-hand gestures can be mimicked and followed out successfully.

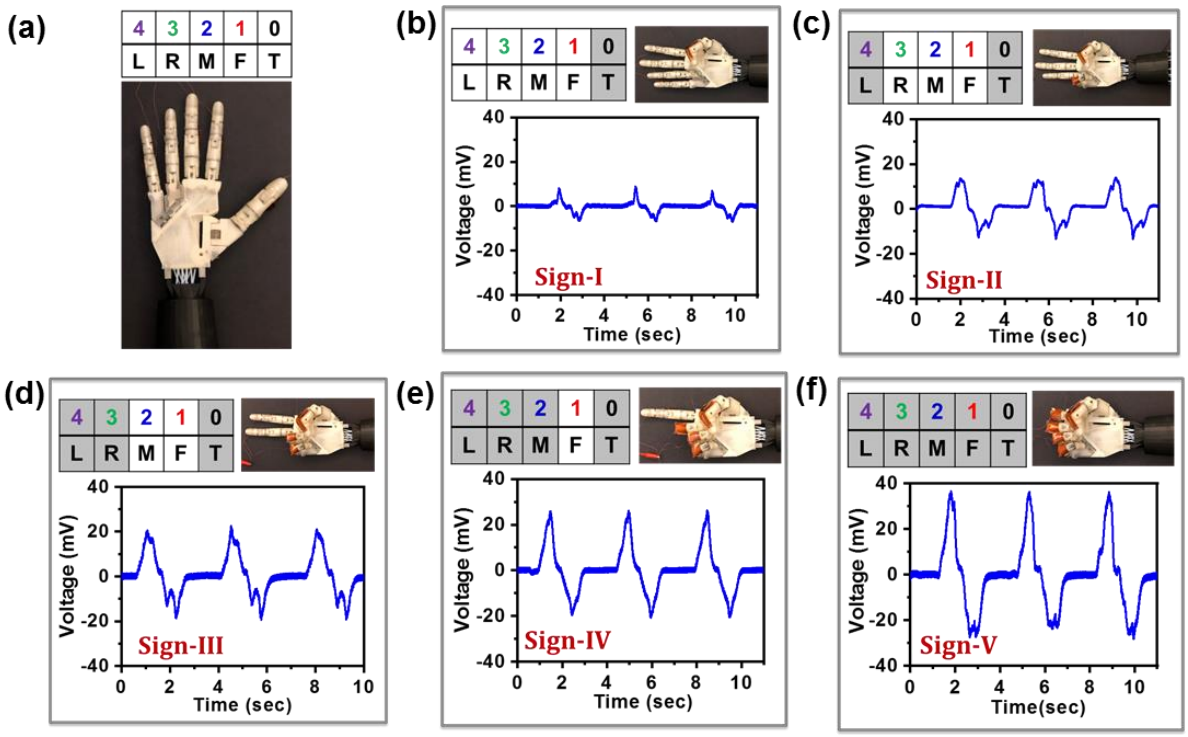

Figure S19. Demonstration of a smart robot sensing platform for enabling technology application from (a) to (f). Five sensors are in serial connection to render larger signals (in terms of amplitude) as more fingers bend.

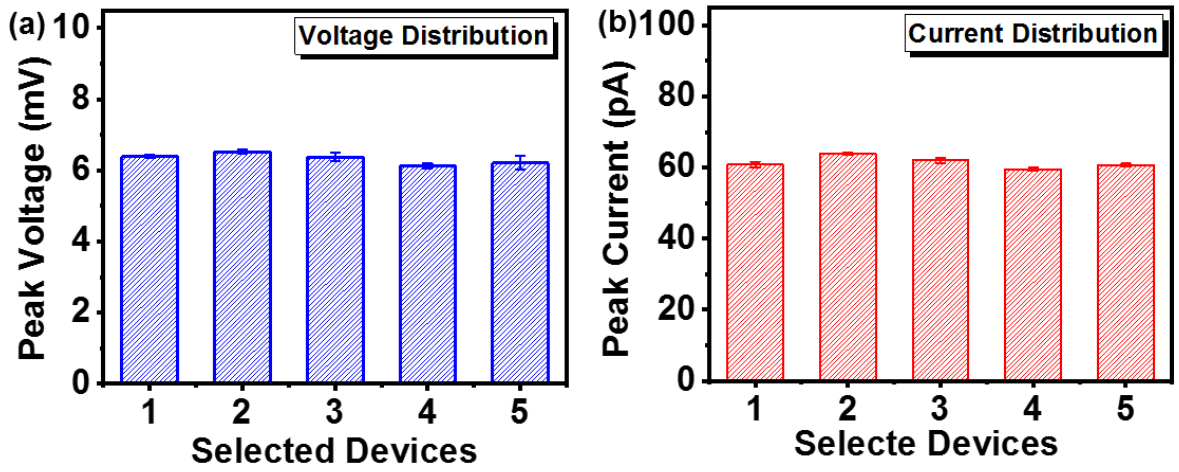

Figure S20. Five SnS_2 PENG devices were selected for the human-robot interface experiments as demonstrated in Figure S19. Before the human-robot demonstration, the output performances of these five devices were tested to show the uniform and consistent voltages and currents under the strain of 0.44%.

Table S1. A comparison of the theoretical and experimental piezoelectric coefficients (d_{11} and d_{33}) of various 2D layered materials reported recently.

2D Materials	Piezoelectric Constant	Theoretical Prediction (pm/V)	Experimental Determination (pm/V)	Fabrication Method/Thickness	Reference
WTe_2	d_{11}	4.39	--	--	[S7]
	d_{33}	6.5	0.7	Exfoliation / Few layer	
WS_2	d_{11}	2.19	--	--	[S5], [S4]
WSe_2	d_{11}	2.79	3.26	CVD / monolayer	[S2], [S3]
$MoTe_2$	d_{11}	7.39	--	--	[S5]
MoS_2	d_{11}	3.73	3.78	CVD / monolayer	[S5], [S6]
	d_{33}	--	1.03		[S8]
$MoSe_2$	d_{11}	4.72	--	--	[S4]
Janus MoSSe	d_{33}	--	0.1	CVD / monolayer	[S1]
In_2Se_3	d_{33}	--	0.34	Exfoliation / monolayer	[S9]
SnS_2	d_{11}	~16	--	--	[S12]
	d_{33}	--	**5**	CVD / Few layer	**This Work***

* Compared with other 2D layered materials, few-layered SnS_2 NSs hold a superior piezoelectric coefficient of d_{33}.

References

[S1] A. Y. Lu, H. Zhu, J. Xiao, C. P. Chuu, Y. Han, M. H. Chiu, C. C. Cheng, C. W. Yang, K. H. Wei, Y. Yang, Y. Wang, D. Sokaras, D. Nordlund, P. Yang, D. A. Muller, M. Y. Chou, X. Zhang, L. J. Li, Nat. Nanotechnol. 12 (2017) 744–749.

[S2] E. Nasr Esfahani, T. Li, B. Huang, X. Xu, J. Li, Nano Energy 52 (2018) 117–122.

[S3] J. H. Lee, J. Y. Park, E. B. Cho, T. Y. Kim, S. A. Han, T. H. Kim, Y. Liu, S. K. Kim, C. J. Roh, H. J. Yoon, H. Ryu, W. Seung, J. S. Lee, J. Lee, S. W. Kim, Adv. Mater. 29 (2017) 1606667.

[S4] K.-A. N. Duerloo, M. T. Ong, and E. J. Reed, 1556 MRS Proceedings (Cambridge University Press) (2013) Mrss13.

[S5] R. Hinchet, U. Khan, C. Falconi, S. Kim, Mater. Today 21 (2018) 611–630.

[S6] S. Kyun, R. Bhatia, T. Kim, D. Seol, J. Ho, H. Kim, W. Seung, Y. Kim, Y. Hee, S. Kim, Nano Energy 22 (2016) 483–489.

[S7] P. Sharma, F. Xiang, D. Shao, D. Zhang, E. Y. Tsymbal A. R. Hamilton J. Seidel, Sci. Adv. 5 (2019) eaax5080.

[S8] C. J. Brennan, R. Ghosh, K. Koul, S. K. Banerjee, N. Lu, E. T. Yu, Nano Lett. 17 (2017) 5464–5471.

[S9] F. Xue, J. Zhang, W. Hu, W. Hsu, A. Han, S. Leung, J. Huang, Y. Wan, S. Liu, J. Zhang, J. He, W. Chang, Z. L. Wang, X. Zhang, L. Li, ACS Nano 12 (2018) 4976–4983.

[S10] W. Wu, L. Wang, Y. Li, F. Zhang, L. Lin, S. Niu, D. Chenet, X. Zhang, Y. Hao, T. F. Heinz, J. Hone, Z. L. Wang, Nature 514 (2014) 470–474.

[S11] H. Song, I. Karakurt, M. Wei, N. Liu, Y. Chu, J. Zhong, Nano Energy 49 (2018) 7–13.

[S12] M. M. Alyörük, Y. Aierken, D. Çaklr, F. M. Peeters, C. Sevik, J. Phys. Chem. C 119 (2015) 23231–23237.

[S13] K. A. N. Duerloo, M. T. Ong, E. J. Reed, J. Phys. Chem. Lett. 3 (2012) 2871–2876.

[S14] J. Yang, A. Wang, S. Zhang, J. Liu, Z. Zhong, L. Chen, Phys. Chem. Chem. Phys. 21 (2019) 132–136.

[S15] Z.L. Wang, Mater. Today, 20 (2017) 74–82.

[S16] M. de Jong, W. Chen, H. Geerlings, M. Asta, K. A. Persson, Sci. Data 2 (2015) 150053.

[S17] I. Petousis, D. Mrdjenovich, E. Ballouz, M. Liu, D. Winston, W. Chen, T. Graf, T. D. Schladt, K. A. Persson and F. B. Prinz, Sci. Data 4 (2017) 160134.